Preferential Interlayer Adsorption Sites in Phyllosilicate Clay Edge Models by Molecular Dynamics Simulation

R. Seaton Ullberg [a], An T. Ta [a], Simon R. Phillpot [a,*]

[a] Department of Materials Science and Engineering, University of Florida, Gainesville, Florida, 32611, United States

Abstract

Phyllosilicate clay minerals have been proposed as a possible buffer material to be used in deep geological repositories containing high-level waste and used nuclear fuel. This work precisely characterizes ion interactions with two types of adsorption sites present in these clays: Mg_{Al}' substitutions and undercoordinated edge surface atoms. A number of unique structural models were considered to represent the diverse local environments that ions in these systems are likely to encounter. Using molecular dynamics simulation with the CLAYFF potential, the spatial distribution, interlayer composition, and residence times of Na^+ and Cl^- ions as radionuclide analogs in pyrophyllite and montmorillonite clay models were investigated to identify the most favorable conditions for sequestration. The most significant factor impacting ion adsorption was found to be the localization of charge density at substitution sites. In a montmorillonite system in which substitution sites were distributed evenly to produce a low charge density, sequestration performance was found to be comparable to pyrophyllite.

Keywords

Molecular dynamics, Montmorillonite, Pyrophyllite, Edge surfaces, Ion adsorption, Interlayer, Charge density

ORCIDs: RSU: 0000-0001-5138-1833; ATT: 0000-0002-2767-8343; SRP: 0000-0002-7774-6535

[*] Corresponding author: sphil@mse.ufl.edu

1. Introduction

Nuclear energy production is an attractive way to satiate the growing energy demands of our society due to its low carbon footprint relative to fossil fuels (Kharecha and Hansen, 2013; Michaelides and Michaelides, 2020; Omri and Saadaoui, 2023). However, the radioactive high-level waste (HLW) and used nuclear fuel (UNF) generated as byproducts in nuclear reactor facilities poses a challenge to the health and safety of surrounding communities and the environment at large. One solution for safe disposal of these dangerous byproducts proposed by multiple national agencies is to use deep geological repositories (Preter, 2002; Bradbury and Baeyens, 2003; Ramírez et al., 2005; Butler, 2010; Altmann et al., 2012). These repositories are the final stage of the nuclear fuel cycle and as such must remain stable and performant on the timescale of one million years (Wall et al., 2022). Clay minerals are stable over these geological timescales and offer additional beneficial properties that make them excellent candidates as buffer materials for these proposed repositories, including high sorption and ion exchange capacity, swelling to limit permeability in water, and high availability in the Earth's crust (Van Olphen, 1991; Ferrage et al., 2005; Rotenberg et al., 2010; Miller and Wang, 2012). In addition to protecting the waste package from its surroundings, the buffer material must be capable of sequestering radionuclides in the event of a container breach (Butler, 2010; Geckeis et al., 2013). Fission products such as iodine-129 and technetium-99 are critical targets for sequestration due to their high mobility in water and tendency to form a variety of polyatomic ions (Meena and Arai, 2017; Zhu et al., 2017; Moore et al., 2020).

Atomic resolution calculations and simulations have proven to be a valuable tool in developing an understanding of engineered buffer materials for HLW and UNF disposal (Wang and Liu, 2012; Sun et al., 2015; Zheng et al., 2023). In particular, molecular dynamics (MD) simulations are capable of probing the dynamical behavior of these materials at the nanoscale. Prior works have used MD simulation in the context of evaluating possible clay buffer materials to predict anion exclusion from hydrated interlayers (Tournassat et al., 2016), the diffusivity of solvated ions (Kosakowski et al., 2008; Ngouana W. and Kalinichev, 2014; Greathouse et al., 2016), and the structure of edge terminations (Newton et al., 2016).

To address the phenomenon of anion exclusion, which is particularly impactful when considering the sequestration of anionic radionuclides such as iodate (IO_3^-) and pertechnetate (TcO_4^-), Tournassat et al. (2016) simulated a (110) terminated montmorillonite nanoparticle adjacent to a region of dilute NaCl solution, referred to as the mesopore. Mg_{Al}' substitutions in their system were randomly distributed throughout three montmorillonite sheets to produce a mean charge density of -0.1 Cm^{-2}, approximately -0.29 electrons per unit cell (e/u.c.), with the stipulation that substitutions could not be located near edge surfaces. The authors used three simulation cells which differed in interlayer water content (and by extension interlayer spacing) to assess the accessibility of the interlayer. The two water-layer system, which was the lowest degree of hydration tested, was found to completely exclude Cl^- ions from the interlayer while both three- and five-layer systems were found to accommodate the anion. In all three systems, Na^+ ions were found to occupy the interlayer at a higher concentration than the mesopore.

Kosakowski et al. (2008) advanced our understanding of interlayer dynamics by determining water and ion diffusivities in mixed Na-Cs-montmorillonite from Monte Carlo and MD simulations. They found that in interlayers with low hydration (monolayer water coverage) Cs^+ ions were immobilized and tended to adsorb to the hexagonal cavities present in the tetrahedral sheet of the montmorillonite. The diffusivities of water and Na^+ ions were found to be similar to each other at all levels of hydration, approaching their bulk values beyond tetralayer water coverage. The clay model used in that study included no edge terminations and had an ordered arrangement of charged substitution sites which limits its applicability to only highly idealized interlayer structures.

Greathouse et al. (2016) expanded upon the work of Kosakowski et al. (2008) by analyzing the effects of net charge, cation species, water content, and temperature in a similar montmorillonite interlayer system. They reported that a charge on the lower end of experimentally reported results (-0.375 e/u.c.) produced a more hydrophobic interlayer condition which led to increased diffusivity of both water and ions relative to a highly charged (-0.75 e/u.c.) clay sheet. Interlayer hydration was only found to have a significant impact on diffusivity in the monolayer water coverage condition. At 2- and 3-layer water coverage, ions become fully hydrated and were found to move more freely through the interlayer. The diffusivity of ions in the interlayer was determined to be almost the same as that in bulk electrolyte solutions of the same concentration. Furthermore, diffusion behavior in the interlayer fluid maintained the trend observed in bulk solution that higher concentrations of electrolyte produce lower diffusion coefficients. However, this study was conducted using an infinite interlayer representation which is a limited analog to real clay nanoparticle systems, which contain edge terminations.

While Kosakowski et al. (2008) and Greathouse et al. (2016) conducted extensive work characterizing the effects of interlayer composition and environmental conditions on ion diffusivity, one structural variable left unevaluated by the authors is the effect of substitutional disorder in the montmorillonite clay sheet. Ngouana W. and Kalinichev (2014) addressed this limitation by introducing three unique structural models of montmorillonite. Their most uniform model, referred to as Uni, contained only octahedral substitutions arranged on a uniform rectangular grid. Two disordered models, RanO and RanTO, contained a random distribution of substitutions limited to the octahedral sheet or mixed between the octahedral and tetrahedral sheets respectively. Restrictions were applied to the RanO and RanTO models to ensure that there was at least one Al site between every substitution site. They reported that the interlayer spacing was similar across all three models and that the same four distinct binding sites for ions on the tetrahedral sheet were active in each model. These findings suggested that substitutional disorder has a negligible impact on the behavior of interlayer ions, However, they did not consider the effect of edge surfaces which, when paired with varying degrees of substitutional disorder, may impact interlayer composition and ionic diffusivity.

In contrast to the previously introduced works which focused their efforts on characterizing behaviors of the interlayer region, Newton et al. (2016) used a combination of ab-initio and classical MD simulations to develop an atomistic model of the montmorillonite edge surface. They found that excess negative charge at edge terminations due to solvent accessible octahedral substitutions tended to produce more disordered edge structures than models with bulk octahedral substitutions. While the work was thorough in its analysis of clay edge surface structures, it did not consider charge-compensating ions which are likely to behave differently in the near-edge and bulk substituted models.

Through this review of the relevant literature, a significant knowledge gap relating specifically to the behavior of ions in the presence of edge-terminated montmorillonite sheets as a function of the arrangement of their octahedral substitution sites has been identified. To close this gap, the current work analyzes a series of MD simulations on clay edge models with substitutions placed specifically to create unique, representative, chemical environments at the edge surfaces and in the deep interlayer region. The resulting simulated trajectories from each model are used to assess how the presence of excess negative charge in different locations relative to the edge termination influences the favorable adsorption sites, interlayer composition, and dynamical behavior of ions.

2. Simulation Cell and Computational Methodology

2.1 Clay Edge Structures

In this work, two structurally similar dioctahedral clays were considered: pyrophyllite and montmorillonite. Both clays have a 2:1 sheet structure in which the outer sheets are silicon tetrahedrally (T) coordinated to oxygen and the inner sheet is aluminum octahedrally (O) coordinated to oxygen. Each of these aluminum octahedral cages contains one oxygen atom that is also bound to a hydrogen atom to form a structural hydroxyl group. These hydroxyl groups are connected to either the top or bottom of the octahedron in a regular alternating pattern. These sheets arrange as repeating TOT units which weakly coordinate across a hydrated interlayer region via van der Waals interactions. Pyrophyllite, an aluminosilicate with the formula $AlSi_2O_5(OH)$, differs from montmorillonite only in the occupancy of its cationic sites. In montmorillonite, partial substitutions of magnesium in the place of octahedral aluminum induce a net negative charge on the structure which is counterbalanced by aqueous cations in the interlayer. In this work, Na^+ was chosen as the counterion, but equally proportioned Na^+/Cl^- pairs were also included to provide a statistically viable sample of ion trajectories to analyze. Montmorillonite can also exist with aluminum substitutions in the tetrahedral silicon sheet, but the effect of Al_{Si}' substitutions is outside the scope of this work. Experimentally, both clays are observed to be monoclinic, but prior works have shown that they can be approximated as orthorhombic in simulation without significantly impacting the dynamics of the system (Ngouana W. and Kalinichev, 2014; Greathouse et al., 2016). Single crystal X-ray diffraction data by Lee and Guggenheim (1981) measured the *a* and *b* lattice parameters of pyrophyllite to be 5.16 Å and 8.97 Å respectively. The *c* axis spans the width of the interlayer region and is thus sensitive to water content; for a dehydrated system the measured value was 9.35 Å.

To best understand the interactions between ions and clay edges in a variety of local environments, four unique simulation cells were created: three montmorillonite systems with unique arrangements of isomorphic Mg_{Al}' substitutions and a pyrophyllite system which served as a charge neutral reference state. Each system consisted of three trans-vacant dioctahedral (empty octahedral site situated on the mirror plane) phyllosilicate clay sheets, three watersaturated interlayers, and a central bulk water mesopore which, in addition, contained all the Na^+ and Cl^- ions at system initialization (Figure 1). The clay sheets were cleaved to expose the 110A termination described by Lavikainen et al. (2015). This termination has consistently been reported as one of, if not the most, favorable edge termination by prior theoretical works (White, 1988; Bickmore et al., 2003; Churakov, 2006; Liu et al., 2014; Newton and Sposito, 2015; Newton et al., 2016; Ta et al., 2023). However, unlike prior works on phyllosilicate edge structures (Churakov, 2006; Tournassat et al., 2016), additional -OH or -H groups were not applied to heal the undercoordinated edge atoms. Instead, molecular water and the Na^+ and Cl^- ions in the system neutralized any localized charge on the edge surfaces. A more detailed description of the coordination of exposed edge atoms is provided in the Supplemental Information. After equilibration, the (100) d-spacing between clay sheets was measured to be 18.9 +/- 0.1 Å, the length of the simulation cell measured along the width of the mesopore was 96.5 +/- 0.2 Å, and the depth measured parallel to the edge surfaces was 46.7 +/- 0.2 Å. These dimensions were comparable to the 3WL system analyzed by Tournassat et al. (2016). Each montmorillonite system contained 96 Mg_{Al}' substitutions, which corresponds to a net charge of -0.33 e/u.c.. A unit cell consisted of two $Al_{0.833}Mg_{0.167}Si_2O_5(OH)$ formula units and had the same lattice dimensions as pyrophyllite. Recent experimental characterization work by Qiu et al. (2020) reported the unit cell charge density of montmorillonite to be in the range of -0.69 to -0.38 e/u.c. Increasing the number of substitutions to create a charge density which is representative of the experimental value would require substitution sites to be placed outside of the distinct locations that were of interest in this work. Therefore, this work employed a substitution scheme which produced a charge density that was as close as possible to the experimental range but still allowed for analysis of the effect of the substitutions' precise location. The pyrophyllite system contained 180 Na^+/Cl^- ion pairs in solution with 5978 water molecules to form a concentration of 1.47 mol/dm^3 which is equivalent to 37% of the solubility limit in water at 298.15 K (Pinho and Macedo, 2005). In the montmorillonite systems, an additional 96 Na^+ ions were included to neutralize the net negative charge induced by Mg_{Al}' substitutions which brought the total concentration up to 45% of the solubility limit. The individual ion concentrations were 1.47 mol/dm^3 for Cl^- and 2.25 mol/dm^3 for Na^+. A higher concentration than is necessary for charge neutralization was chosen to provide ample data in the resulting simulated trajectories.

The three montmorillonite systems under investigation in this work are referred to as MMT-central, MMT-edge, and MMT-equidistant. The suffix describes the arrangement of $\mathrm{Mg}_{\mathrm{Al}}'$ substitutions within the clay sheet. In the MMT-central system all substitutions were localized to the center of the interlayer region, i.e., as far away as possible from the mesopore edge. In the MMT-edge system the opposite scenario was investigated as substitutions were placed directly on the terminated clay edges. The MMT-equidistant system represented an intermediate case in which the substitutions were evenly spaced throughout the sheets so as not to create a highly localized charge density at the edge or in the center.

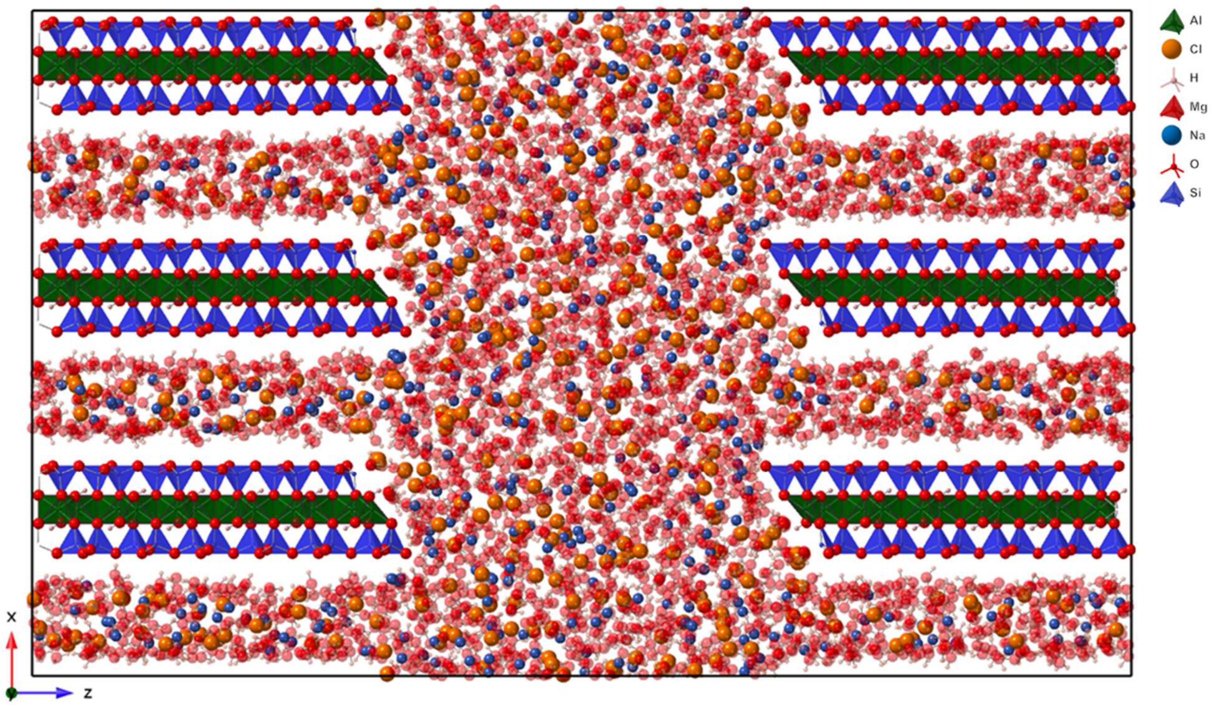

Figure 1: Snapshot of the fully equilibrated pyrophyllite simulation cell. For clarity, the water molecules are rendered with low opacity. Atom types illustrated as follows: Na^+ (blue), Cl^- (orange), O (red), Octahedral Al (green), Tetrahedral Si (blue), H (pink).

2.2 Molecular Dynamics Simulations

All molecular dynamics simulations in this work were executed in LAMMPS (Plimpton, 1995; Thompson et al., 2022) and all initial atomic coordinate files were generated using the Moltemplate software package (Jewett et al., 2021). The mesopore and interlayer regions were packed with 1.0 g/cm^3 of water and the Na^+/Cl^- ions were arranged on a grid in the mesopore and allowed to diffuse out during equilibration so as not to preemptively bias the composition of the interlayers. Interactions within the clay sheet were modeled using the CLAYFF potential developed by Cygan et al. (2004). Water in the mesopore and interlayer regions was modeled using the SPC/e potential of Berendsen et al. (1987) with the SHAKE algorithm (Ryckaert et al., 1977) turned off. Our preliminary benchmark calculations (included in the Supplemental Information) showed that disabling SHAKE results in better agreement with experimental measurements of bulk water diffusivity. Lennard-Jones parameters for aqueous Na^+ and Cl^- ions were adopted from the work of Smith and Dang (1994). Non-bonded interactions between dissimilar species were fit using LAMMPS' arithmetic mixing strategy. Coulombic contributions were evaluated using the Ewald sum method. The boundaries of the simulation cell were treated as periodic in all dimensions. Therefore, when describing phenomena occurring in the "center" of the clay sheet, they will appear on the far left and right of the visible simulation cell because the cell is centered on the mesopore.

Equilibration was carried out in multiple phases. The first was an energy minimization step in which the total energy was converged to a tolerance of 10^{-6} kcal/mol. Using the energy minimized system as a starting point, a simulation in the NVT ensemble was run for 2.0 ns with a timestep of 0.5 fs and a target temperature of 300 K. During this first NVT phase only water molecules were allowed to move. Then, a second 2.0 ns phase was conducted in which both ions and water molecules were allowed to move freely. Following the NVT phase, an NPT simulation was conducted for another 2.0 ns, again using a timestep of 0.5 fs, with a pressure target of 1 atm and a temperature target of 300 K. During the NPT phase the volume of the cell was allowed to relax anisotropically. Throughout all equilibration phases the clay sheets were made rigid using the LAMMPS fix *setforce,* following the precedent set by similar works (Rotenberg, 2007; Hedström and Karnland, 2012; Hsiao and Hedström, 2015). This implementation allows the constant pressure algorithm to optimize the interlayer spacing without shifting atoms in the clay sheet relative to each other. Benchmark calculations showed that when the rigid constraint was not applied during equilibration the clay sheets would oscillate in a wave-like motion that did not settle down over the course of the equilibration. It is expected that this effect is an artifact of system size, and the simulations would eventually stabilize if a wider clay sheet were investigated; however, the computational cost of such large simulations is prohibitive. After equilibration the *setforce* restriction was applied only to the octahedral sheet to allow more flexibility in the basal planes. The production simulations were conducted in the NVT ensemble for a duration of 10 ns using a timestep of 0.5 fs and a temperature target of 300 K.

3. Results

3.1 Spatial Distribution of Na^+ and Cl^- Ions

This section provides a qualitative overview of the features in each clay model that are evident from visual inspection of the ionic trajectories. In subsequent sections, quantitative analyses expand upon these observations to robustly characterize the behavior of ions across each environment. Figure 2 illustrates the MD trajectories of the Na^+ (blue) and Cl^- (orange) ions over the course of a 10 ns production simulation in NVT. Green points highlight the position of the octahedral Al sheet. In montmorillonite systems, red 'X's denote the positions of $\mathrm{Mg_{Al}}'$ substitution sites within the octahedral sheet. All other species were excluded from this visualization. Vertical dashed lines delineate the interlayer/mesopore boundary (IMB) which was defined as the position of the outermost oxygen on the clay edge termination. The figure was composed by superimposing the *xz*-plane projected positions of each ion in 200 snapshots exported every 50 ps. The positions were plotted with low opacity at each snapshot so that regions which accumulate ions appeared as bright hotspots and regions with a lower ion density appeared to be more dispersed. Each subplot corresponds to a unique system.

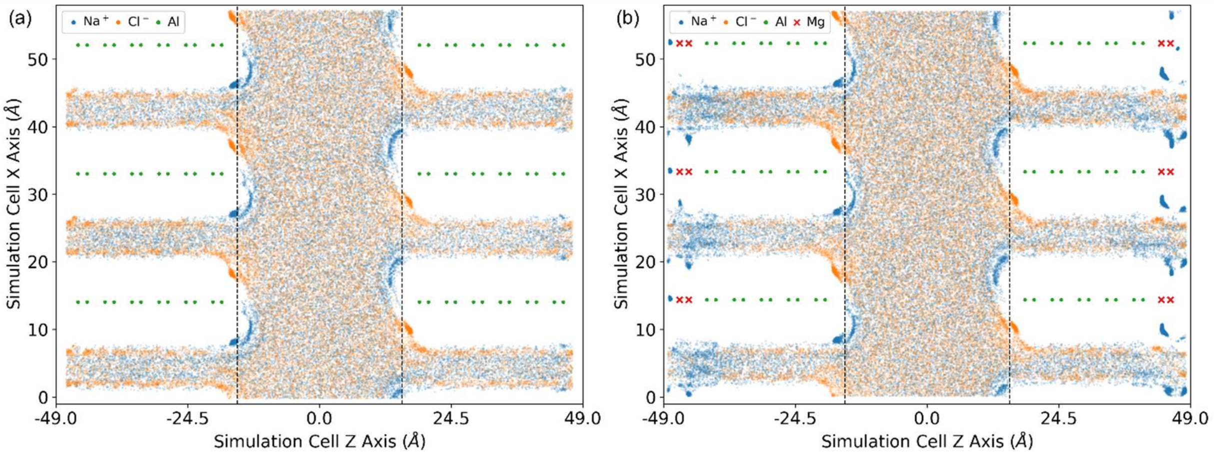

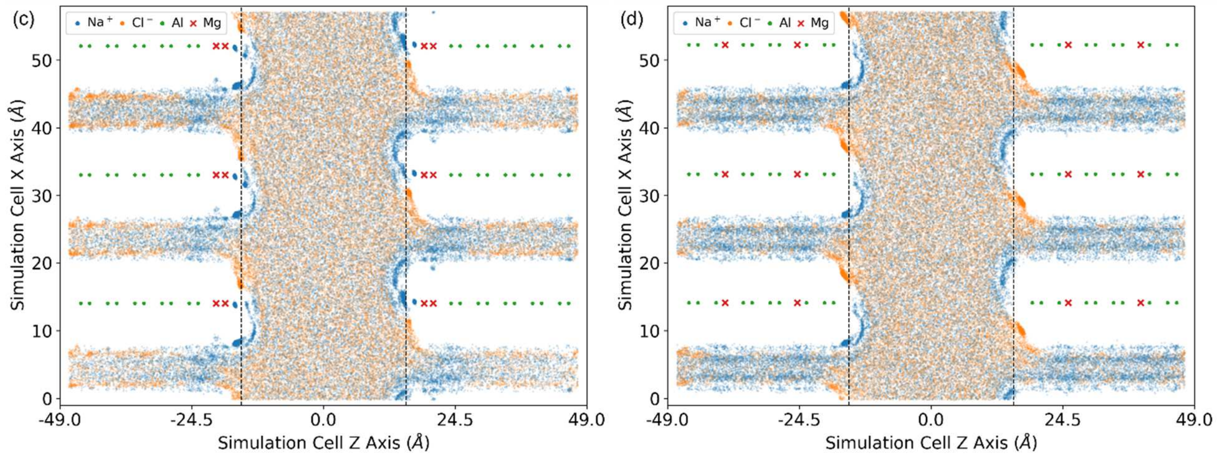

Figure 2: Positions of Na$^+$ (blue) and Cl$^-$ (orange) ions projected onto the *xz*-plane of the simulation cell. Positions taken from 200 snapshots over the course of a 10 ns NVT simulation are superimposed. Octahedral Al is shown in green and Mg_{Al}' substitutions are denoted by red 'X's. The vertical dashed lines represent the interlayer mesopore boundary. Each subplot corresponds to a unique system: (a) Pyrophyllite, (b) MMT-central, (c) MMT-edge, (d) MMT-equidistant.

One feature evident in all subplots of Figure 2 is the agglomeration of both Na$^+$ and Cl$^-$ ions on each edge termination, just outside of the IMB. This feature is most clearly illustrated in Figure 2a which depicts pyrophyllite. A symmetrical split of Na$^+$ density around the leading edge (projecting into the mesopore) and Cl$^-$ density near the trailing edge is consistent with the choice to leave any dangling bonds created during the edge cleavage unhealed. This finding is also supported by prior work from Ta et al. (2023) in which density functional theory calculations identified a negative partial charge on the undercoordinated oxygen on the leading edge and a positive partial charge on the undercoordinated Si on the trailing edge. In Figures 2b-d, the impact of Mg_{Al}' substitutions on the distribution of ions can be clearly contrasted with their distribution in the charge neutral pyrophyllite system.

Figure 2b illustrates the MMT-central system. This system had the highest charge density (four substitutions in close proximity due to periodic boundary conditions) and its substitutions were located furthest from the IMB. In this system, Na$^+$ ions were observed to adsorb onto the outer tetrahedral sheet. Visualizations of a typical arrangement of the adsorbed Na$^+$ ions in this cluster and others are provided in the Supplemental Information. Note that because the simulation cell was defined as periodic in all dimensions, there are four substitution sites directly adjacent along the *z*-axis in each clay sheet. It can be seen that the ions were drawn towards the basal oxygen nearest each substitution site and occasionally penetrated the basal plane in the center of the four aligned substitutions where charge density was highest. Furthermore, it is evident that in the interlayer region adjacent to the adsorbed Na^+ ions, small but dense clusters of Cl^- ions formed to neutralize the localized charge density. However, these anions remained solvated in the interlayer.

Figure 2c, which details the MMT-edge system, is the opposite to the previously discussed MMT-central system in that its substitution sites were placed as close as possible to the IMB. This arrangement resulted in a lower charge density because the substitutions on each side of the mesopore were no longer adjacent through the periodic boundary, but similar features were identifiable. Clusters of Na^+ ions along the basal plane in the interlayer nearest to the Mg_{Al}' substitution sites were still evident. These cations underwent a similar adsorption process in which they densely clustered around the basal oxygen atoms nearest each substitution site, but full penetration into the tetrahedral sheet was never observed. The interior interlayer regions adjacent to these surface adsorbed ions did not form the same dense charge-compensating clusters of Cl^- ions observed in the MMT-central system. Additionally, there was a markedly diminished amount of Na^+ ions in the deep interlayer region on account of the lack of electrostatic driving force past the IMB.

The third montmorillonite system under consideration, MMT-equidistant, is presented in Figure 2d. Despite having the same overall number of substitutions as the other montmorillonite systems, this case represents the lowest charge density (aside from neutral pyrophyllite) due to the large distance between substitution sites. Additionally, this system's substitutions were evenly spread between the IMB and central interlayer region which offers an interesting opportunity to study the behavior of ions outside the range of influence of the edge termination. Perhaps most evident in Fig. 2d is the lack of Na^+ adsorption onto the clay's basal planes which was seen in other montmorillonite systems. Na^+ ions in this system tended to form a diffuse cloud in the interlayer region centered around each substitution site rather than converging to a fine point. There was no agglomeration of Cl^- ions in the interlayer to counterbalance the presence of Na^+ and the distribution of ions near the edge terminations was not visually distinguishable from that of pyrophyllite.

3.2 Localized Concentration of Na^+ and Cl^- Ions

To further characterize the composition of each system, the concentration of both Na$^+$ and Cl$^-$ was projected along the width of the simulation cell as shown in Figure 3. Concentration was plotted relative to the baseline value of pyrophyllite and montmorillonite systems respectively. Recall that the pyrophyllite system was packed with ions to achieve 37% of the solubility limit of water, but in montmorillonite systems additional Na$^+$ ions were needed to neutralize Mg_{Al}' substitution sites, bringing the concentration to 45% of the solubility limit. Measurements of concentration were discretized by dividing the simulation cell into 25 bins along its *z*-axis and calculating the concentration for each volume element.

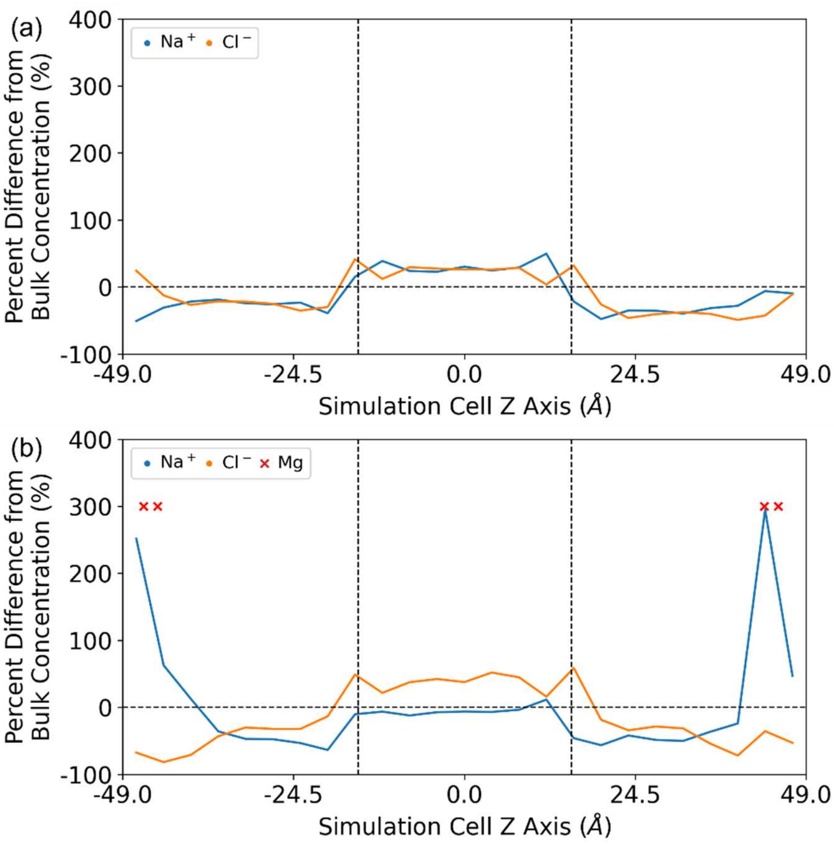

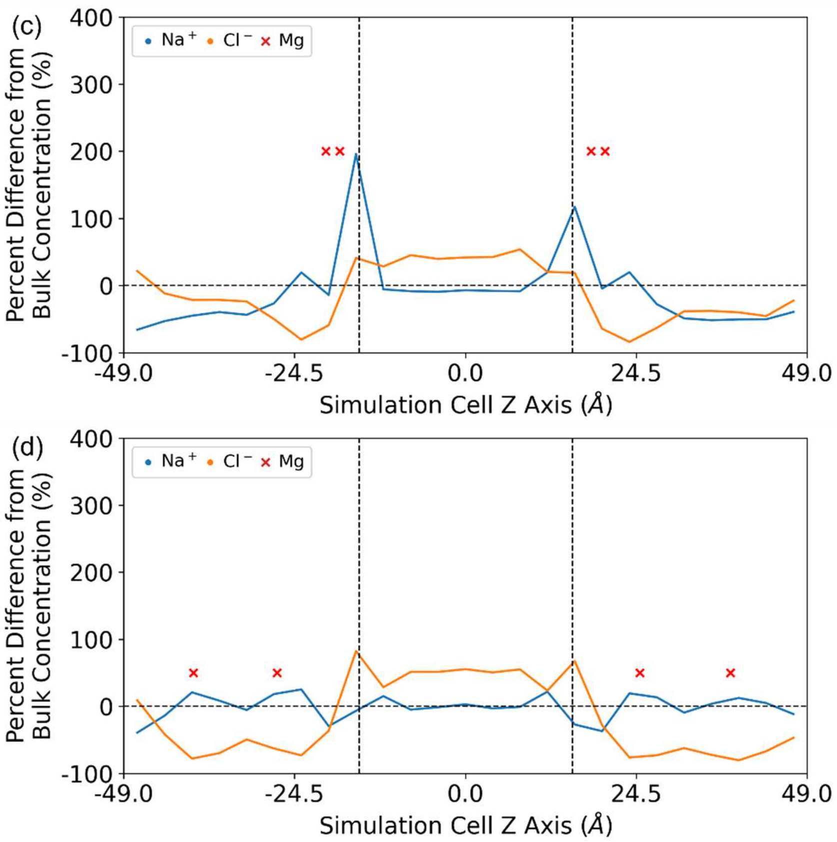

Figure 3: Concentration of Na^+ (blue) and Cl^- (orange) ions relative to their bulk values projected along the *z*-axis of the simulation cell. Vertical dashed lines denote the IMB and red 'X's represent the positions of Mg_{Al}' substitutions. Each subplot corresponds to a unique system: (a) pyrophyllite, (b) MMT-central, (c) MMT-edge, (d) MMT-equidistant.

One trend which becomes evident from inspection of Figure 3a is the tendency for the ion concentrations in the interlayer to be lower than in the mesopore. The concentration of the two ions was nearly identical throughout the simulation cell except for the near-IMB region where Na^+ and Cl^- peaks separated and reach concentrations greater than the bulk value. This behavior closely resembles that identified in Figure 2a where the Na^+ clusters formed closer to the mesopore on the leading edge of the IMB and the Cl^- clusters formed closer to the interlayer.

Concentration profiles in the MMT-central system (Figure 3b) retained the strong Na^+ peaks around Mg_{Al}' substitution sites found in Figure 2b. However, this visualization shows that Cl^- concentration increased only slightly in the same region indicating that the observed compensating clusters in the adjacent interlayer were more diffuse. Throughout the remainder of the interlayer, concentrations of both ions remained below the bulk concentration. In the mesopore, Na^+ was found to be at bulk concentration levels while Cl^- was in excess.

The MMT-edge concentration profiles presented in Figure 3c display sharp peaks of both Na^+ and Cl^- near the IMB. On the interior side of the IMB, directly adjacent to the Mg_{Al}' substitution sites, a significant drop in the concentration of Cl^- was observed. This finding contrasts with the behavior of the MMT-central system where Cl^- accumulated with Na^+ at the substitution sites to neutralize local charge density. This behavior is likely due to the presence of strongly adsorbed Na^+ ions on the edge surface which act as a sink for incoming Cl^- anions that would otherwise be drawn deeper into the interlayer. Throughout the interlayer, the concentration of both ions remained below the bulk value although Cl^- tended to be higher than Na^+ after the initial drop at the substitution sites. In the mesopore, Cl^- concentration was found to be in excess of the bulk value.

In Figure 3d, the MMT-equidistant concentration profile was unique in that the Na^+ concentration in the interlayer was only slightly greater than the bulk value near substitution sites. Despite the presence of Mg_{Al}' substitution sites which provide an electrostatic driving force for Na^+ to cluster in the interlayer, the cation was found in nearly equal proportion within the mesopore and near the edge terminations. The behavior of Cl^- near substitution sites was like that of the MMT-edge profile; Cl^- was clearly disfavored near substitutions and displayed a significant decrease in concentration where Na^+ concentration rose. The concentration of Cl^- rose higher than Na^+ near the IMB although the peaks were identical in location to those found in pyrophyllite.

3.3 Residence Time of Adsorbed Na^+ and Cl^- Ions

In order to capture the dynamical behavior of these phyllosilicate clay systems at edge surfaces and substitution sites, Figure 4 reports the distribution of residence times of ions in equally sized slices along the simulation cell. Residence times were derived from ion trajectories exported every 1 ps over the course of the final 1 ns of simulation time. A residence event is triggered when an ion enters a bin it did not occupy in the prior snapshot and continues until the ion moves to another bin. Each event for each ion is reported in Figure 4 which means that there are more data points than ions because most ions pass through multiple bins over the course of the simulation. When interpreting these results, it is important to consider how the geometry of the simulation cell intersects with the boundaries of each bin. For bins in the interlayer, the clay sheets reduce the total traversable volume. This reduction in traversable volume is not present for mesopore bins. The effect of this difference is that residence times in the interlayer are artificially lower than those in the mesopore because ion motion in the interlayer is primarily two dimensional while ions in the mesopore have a full range of motion. It is not expected that this effect hinders the analysis of residence times because it is not strong enough to mask the electrostatic interactions between ions and substitution/edge sites as evidenced in Figure 4. Furthermore, it is important to note that the most frequently recorded residence time in each bin is just 1 ps because that is the minimum step size and the ions are flowing freely. To highlight the more interesting longer residence events, a curve is superimposed over each subplot which represents the 95th percentile residence time for each ion type in each bin.

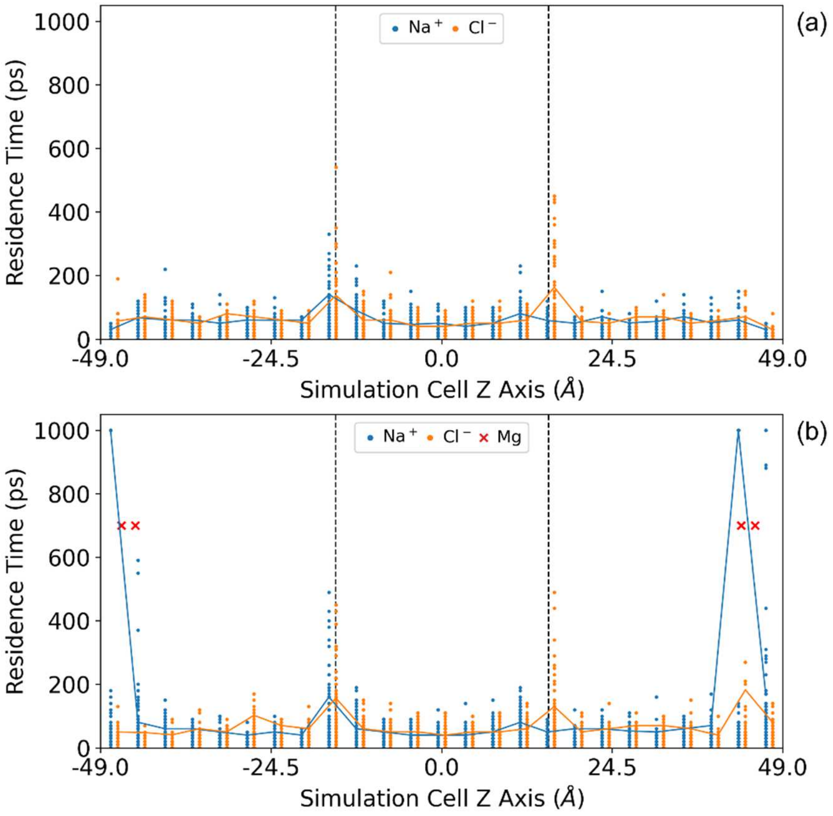

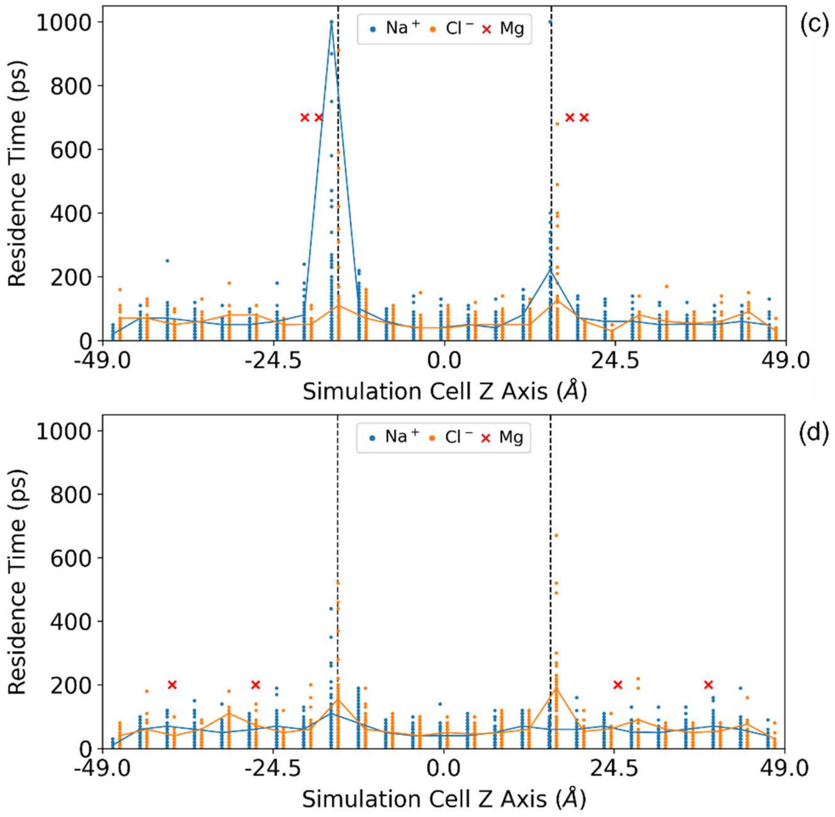

Figure 4: Residence times of Na$^+$ (blue) and Cl$^-$ (orange) ions projected along the *z*-axis of the simulation cell. Residence times are calculated in 25 equally sized bins. For clarity, Na$^+$ and Cl$^-$ data points have been offset from each other about the center of each bin. Vertical dashed lines denote the IMB and red 'X's represent the positions of $\mathrm{Mg_{Al}}'$ substitutions. Each subplot corresponds to a unique system: (a) pyrophyllite, (b) MMT-central, (c) MMT-edge, (d) MMT-equidistant.

All subplots of Figure 4 indicate that a small number of Na$^+$ and Cl$^-$ ions remained adsorbed to the edge surface for at least 400 ps. This finding is consistent with the bright hotspots of Cl$^-$ on the trailing edge and Na$^+$ on the leading edge of each clay sheet presented in Figure 2. Interestingly, the residence times of both ions were not always equal despite similar hotspots for each shown in Figure 2. While it is expected that both Na$^+$ and Cl$^-$ would tend to congregate at edge surfaces to heal the undercoordinated oxygen and silicon atoms respectively, it is likely that the difference in residence times between Cl$^-$-Si and Na$^+$-O pairs is due to geometric features of the edge structure. Based on the CLAYFF parameters which drive these simulations, the magnitude of the partial charge on the undercoordinated basal oxygen and the undercoordinated tetrahedral silicon are equivalent. Pairing this with the fact that equilibrium distances between both pairs are similar, differences in electrostatic interaction strength can be eliminated as a contributing factor. Recalling the arrangement of the edge structure from Figure 1, it can be seen that the undercoordinated oxygen projects out into the mesopore and is highly exposed to water while the undercoordinated silicon is largely insulated by the overhanging edge of the clay sheet and is accessible only through a small concave region adjacent to the interlayer. Therefore, it follows that Na^+ ions being drawn to the undercoordinated oxygen would be more frequently carried away by highly mobile water molecules than their less exposed Cl^- counterparts.

In the pyrophyllite system (Figure 4a), residence times throughout the interlayer and mesopore were consistently less than 200 ps. It is only near the IMB that prolonged residence was observed. Aside from the small set of strongly interacting Cl^- outliers, Na^+ ions tended to reside on the edge for a maximum of 300 ps and less strongly bound Cl^- ions for a maximum of 500 ps. Furthermore, it is evident that residence times of both species were elevated in the mesopore bins directly adjacent to those centered on the IMB. However, the same effect was not observed on the interlayer side of the IMB. This suggests that the electrostatic influence of the edge terminations extends approximately 4 Å into the mesopore and asymmetrically affects mesopore ions.

Figure 4b illustrates how Mg_{Al}' substitutions in the MMT-central system significantly increased the residence times of Na^+ ions in the interlayer. A small number of Na^+ ions adjacent to substitution sites remained static for the full 1 ns duration of the data collection period. The precise arrangement of these low-mobility cations can be found in the Supplemental Information. In addition to this small group of strongly interacting ions, Cl^- ions in the same region were observed to also increase in residence time to over 200 ps – more than twice the value recorded throughout the rest of the interlayer. This increase in Cl^- residence time reflects the presence of the charge compensating clusters of Cl^- ions adjacent to Na^+ interlayer adsorption sites shown in Figure 2b. Near the IMB, residence times were consistent with those observed in pyrophyllite.

When substitutions were placed on the edge surface, the differences in residence time profiles relative to the neutral pyrophyllite system could only be distinguished along the IMB. Along the edge surface, a select number of Na^+ cations were observed to remain adsorbed for the full 1 ns data collection period. In Figure 4c, residence times for both ionic species were observed to peak near the IMB and remained below 200 ps throughout the rest of the system. A more subtle difference from Figure 4a is that the increased residence times near the IMB were no longer asymmetrically distributed on the mesopore side, but now extended into the interlayer side as well. This behavior was expected due to the presence of the Mg_{Al}' substitutions driving cations to congregate in the interlayer just past the trailing edge of each clay sheet termination. Another difference from the pyrophyllite case is that the ions in the MMT-edge system tended to produce a wider range of residence times. In pyrophyllite, there were very few points above 300 ps aside from the IMB adjacent Cl^- ions, but in MMT-edge the distribution was split more evenly between 0 and 1000 ps for both ionic species.

In Figure 4d, the presence of evenly distributed substitution sites in the MMT-equidistant system produced a profile of residence times that was almost identical to those found in pyrophyllite. Even in bins containing Mg_{Al}' sites, the residence times for either ion did not exceed 200 ps. Near the IMB, the same trends were observed where a select few Cl^- ions tended to remain adsorbed at the edge surface for over 500 ps while Na^+ ions were more mobile and had a peak residence time of approximately 400 ps. Figure 4d illustrates that the low charge density associated with this arrangement of substitutions was insufficient to retain ions in the interlayer.

4. Discussion

Comparing the results across each system of interest, it is evident that localized charge density is the primary driving force controlling the distribution of ions. Two sources of charge, unhealed edge terminations and Mg_{Al}' substitution sites, control the electrostatics in each system. The distribution of ions around edge terminations was broadly consistent with Na^+ favoring the leading edge of each termination (closest to the mesopore) and Cl^- congregating on the tailing edge (closest to the interlayer). However, the magnitude of ion clusters at clay edges could be influenced by the presence of Mg_{Al}' substitutions. As evidenced by Figs. 2c and 3c, the MMT-edge system sequestered a greater amount of Na^+ ions at edge terminations than all other systems due to the presence of charged substitutions in close proximity. In other montmorillonite systems where substitution sites were placed far from the edges, the distribution and number of ions adsorbed on the edge facets was close to that of the charge neutral pyrophyllite system. Substitution sites, alternatively, may be positioned in order to drive an influx of ions into the interlayer. High charge density in the MMT-central systems led to not only an influx of Na^+, but also a secondary cluster of Cl^- which served to counterbalance the cations adsorbed to the basal plane of the clay sheet. In the MMT-equidistant system, which was lower in charge density, such strong accumulation of Na^+ was not observed which in turn eliminated the need for a secondary cluster of compensating Cl^-. In fact, from inspection of Figures 2d and 3d, the MMT-equidistant system was found to exclude Cl^- from the interlayer more so than any other. When residence times were considered, it became clear that both the pyrophyllite (Figure 4a) and MMT-equidistant (Figure 4d) systems failed to capture ions in the interlayer for any significant duration. Alternatively, the MMT-central system was capable of drawing ions into the interlayer and sequestering them on the order of 1 ns as can be seen in Figure 4b. Interestingly, MMT-central was capable of retaining not only Na^+ as one would expect from simple electrostatic interactions, but also Cl^- which was observed to have elevated residence times upwards of 200 ps. This suggests that a higher charge density may be necessary to adsorb ions using a montmorillonite clay base if special care is not taken to design the sheet in such a way that substitutions tend to be clustered.

In the context of clay buffer materials, these results help researchers better understand the criteria to consider when manufacturing or modifying the base clay. The results of this work have shown that even without any octahedral substitutions in the clay sheet, exposed edge surfaces are able to consistently sequester both cations and anions from solution. This finding suggests that during processing, it may be optimal to minimize the volume of individual clay particles in a suspension so that the maximal amount of surface area is exposed and available for ions to adsorb to. However, strides may still be made to improve sequestration performance within the interlayer. Our simulations predict that an even distribution of substitution sites throughout a clay sheet significantly underperforms a sheet in which the substitutions are clustered close together despite both sheets having the same net charge. While this may be a more difficult variable to tune from a synthesis perspective, the finding opens the door to future research into methodologies that can offer better control over the precise arrangement of substitutions in the octahedral sheet. Furthermore, this work does not consider how Al_{Si}' substitutions in the tetrahedral sheet may change the sequestration performance of the clay. In future work, an investigation into this additional substitution type or a combination of both tetrahedral and octahedral substitutions may paint a fuller picture of ion capture in hydrated phyllosilicate clay edge models.

5. Conclusions

By comparing simulations of distinct clay edge models with varying electrostatic environments, the effect of both unhealed edge surfaces and Mg_{Al}' substitution sites on ion sequestration can be characterized. It is evident that regardless of the distribution or presence of octahedral substitution sites, edge terminations can effectively retain both anionic and cationic species. In the absence of additional local charge from substitution sites these edge terminations can adsorb ions for durations on the order of 400 ps. However, the inclusion of nearby substitutions drastically increased the performance to 1 ns which was the longest duration tested. Furthermore, particular arrangements of octahedral substitutions can contribute to varying levels of ion concentration and selectivity in the interlayer. The arrangement found to limit Cl^- penetration most was the evenly distributed MMT-equidistant which exhibited drastically reduced Cl^- concentration in the interlayer relative to the mesopore. An alternative high local charge density configuration, MMT-central, was found to draw both Na^+ and Cl^- into the deep interlayer and effectively retain Na^+ ions for up to 1 ns. As expected, charge neutral pyrophyllite was identified as the least selective in controlling specific ion concentrations in the interlayer.

These findings are valuable in the context of radionuclide sequestration. Building on the results of this work, two key design considerations for clay buffer materials have been identified: maximizing exposed surface area can result in enhanced sequestration performance under any substitution conditions, and evenly distributed substitutions in the interlayer enhance anion exclusion relative to systems with high localized charge density.

Acknowledgements

The authors would like to thank Nathalie A. Wall, Emily Maulden, Elizabeth J. Gager, Juan C. Nino (University of Florida), Carolyn I. Pearce and James E. Szecsody (PNNL) for their invaluable insight and conversations pertaining to this study. We also acknowledge University of Florida Research Computing for providing computational resources and support.

Data Availability

Essentially all data is contained in this manuscript and Supplemental Information, though, additional details can be available on reasonable request.

Funding

This work was supported by U.S. DOE Office of Nuclear Energy's Nuclear Energy University Program under grant DE-NE0008952.

References

Altmann, S., Tournassat, C., Goutelard, F., Parneix, J.-C., Gimmi, T., Maes, N., 2012. Diffusion-driven transport in clayrock formations. Appl. Geochem., Fundamental processes of radionuclide migration in the geosphere 27, 463–478. https://doi.org/10.1016/j.apgeochem.2011.09.015

Berendsen, H.J.C., Grigera, J.R., Straatsma, T.P., 1987. The missing term in effective pair potentials. J. Phys. Chem. 91, 6269–6271. https://doi.org/10.1021/j100308a038

Bickmore, B.R., Rosso, K.M., Nagy, K.L., Cygan, R.T., Tadanier, C.J., 2003. Ab Initio Determination of Edge Surface Structures for Dioctahedral 2:1 Phyllosilicates: Implications for Acid-Base Reactivity. Clays Clay Miner. 51, 359–371. https://doi.org/10.1346/CCMN.2003.0510401

Bradbury, M., Baeyens, B., 2003. Near Field sorption Data Bases for Compacted MX-80 Bentonite for Performance Assessment of a High-Level Radioactive Waste Repository in Opalinus Clay Host Rock. U.S. Department of Energy Office of Scientific and Technical Information.

Butler, D., 2010. France digs deep for nuclear waste. Nature 466, 804–805. https://doi.org/10.1038/466804a

Churakov, S.V., 2006. Ab Initio Study of Sorption on Pyrophyllite: Structure and Acidity of the Edge Sites. J. Phys. Chem. B 110, 4135–4146. https://doi.org/10.1021/jp053874m

Cygan, R.T., Liang, J.-J., Kalinichev, A.G., 2004. Molecular Models of Hydroxide, Oxyhydroxide, and Clay Phases and the Development of a General Force Field. J. Phys. Chem. B 108, 1255–1266. https://doi.org/10.1021/jp0363287

Ferrage, E., Lanson, B., Sakharov, B.A., Drits, V.A., 2005. Investigation of smectite hydration properties by modeling experimental X-ray diffraction patterns: Part I. Montmorillonite hydration properties. Am. Mineral. 90, 1358–1374. https://doi.org/10.2138/am.2005.1776

Geckeis, H., Lutzenkirchen, J., Polly, R., Rabung, T., Schmidt, M., 2013. Mineral–Water Interface Reactions of Actinides. Chem. Rev. https://doi.org/10.1021/cr300370h

Greathouse, J.A., Cygan, R.T., Fredrich, J.T., Jerauld, G.R., 2016. Molecular Dynamics Simulation of Diffusion and Electrical Conductivity in Montmorillonite Interlayers. J. Phys. Chem. C 120, 1640–1649. https://doi.org/10.1021/acs.jpcc.5b10851

Hedström, M., Karnland, O., 2012. Donnan equilibrium in Na-montmorillonite from a molecular dynamics perspective. Geochim. Cosmochim. Acta. https://doi.org/10.1016/j.gca.2011.11.007

Hsiao, Y.-W., Hedström, M., 2015. Molecular Dynamics Simulations of NaCl Permeation in Bihydrated Montmorillonite Interlayer Nanopores. J. Phys. Chem. C 119, 17352–17361. https://doi.org/10.1021/acs.jpcc.5b01169

Jewett, A.I., Stelter, D., Lambert, J., Saladi, S.M., Roscioni, O.M., 2021. Moltemplate: A Tool for Coarse-Grained Modeling of Complex Biological Matter and Soft Condensed Matter Physics | Elsevier Enhanced Reader. J. Mol. Biol. https://doi.org/10.1016/j.jmb.2021.166841

Kharecha, P.A., Hansen, J.E., 2013. Prevented Mortality and Greenhouse Gas Emissions from Historical and Projected Nuclear Power. Environ. Sci. Technol. 47, 4889–4895. https://doi.org/10.1021/es3051197

Kosakowski, G., Churakov, S.V., Thoenen, T., 2008. Diffusion of Na and Cs in Montmorillonite. Clays Clay Miner. 56, 190–206. https://doi.org/10.1346/CCMN.2008.0560205

Lavikainen, L.P., Hirvi, J.T., Kasa, S., Schatz, T., Pakkanen, T.A., 2015. Stability of dioctahedral 2:1 phyllosilicate edge structures based on pyrophyllite models. Theor. Chem. Acc. 134, 112. https://doi.org/10.1007/s00214-015-1715-6

Lee, J.H., Guggenheim, S., 1981. Single crystal X-ray refinement of pyrophyllite-1Tc. Am. Mineral. 66, 350–357.

Liu, X., Cheng, J., Sprik, M., Lu, X., Wang, R., 2014. Surface acidity of 2:1-type dioctahedral clay minerals from first principles molecular dynamics simulations. Geochim. Cosmochim. Acta 140, 410–417. https://doi.org/10.1016/j.gca.2014.05.044

Meena, A.H., Arai, Y., 2017. Environmental geochemistry of technetium. Environ. Chem. Lett. 15, 241–263. https://doi.org/10.1007/s10311-017-0605-7

Michaelides, E.E., Michaelides, D.N., 2020. Impact of nuclear energy on fossil fuel substitution. Nucl. Eng. Des. 366, 110742. https://doi.org/10.1016/j.nucengdes.2020.110742

Miller, A.W., Wang, Y., 2012. Radionuclide Interaction with Clays in Dilute and Heavily Compacted Systems: A Critical Review. Environ. Sci. Technol. 46, 1981–1994. https://doi.org/10.1021/es203025q

Moore, R.C., Pearce, C.I., Morad, J.W., Chatterjee, S., Levitskaia, T.G., Asmussen, R.M., Lawter, A.R., Neeway, J.J., Qafoku, N.P., Rigali, M.J., Saslow, S.A., Szecsody, J.E., Thallapally, P.K., Wang, G., Freedman, V.L., 2020. Iodine immobilization by materials through sorption and redox-driven processes: A literature review. Sci. Total Environ. 716, 132820. https://doi.org/10.1016/j.scitotenv.2019.06.166

Newton, A.G., Kwon, K.D., Cheong, D.-K., 2016. Edge Structure of Montmorillonite from Atomistic Simulations. Minerals 6, 25. https://doi.org/10.3390/min6020025

Newton, A.G., Sposito, G., 2015. Molecular Dynamics Simulations of Pyrophyllite Edge Surface: Structure, Surface Energies, and Solvent Accessibility. Clays Clay Miner. 63, 277–289. https://doi.org/10.1346/CCMN.2015.0630403

Ngouana W., B.F., Kalinichev, A.G., 2014. Structural Arrangements of Isomorphic Substitutions in Smectites: Molecular Simulation of the Swelling Properties, Interlayer Structure, and Dynamics of Hydrated Cs–Montmorillonite Revisited with New Clay Models. J. Phys. Chem. C 118, 12758–12773. https://doi.org/10.1021/jp500538z

Omri, E., Saadaoui, H., 2023. An empirical investigation of the relationships between nuclear energy, economic growth, trade openness, fossil fuels, and carbon emissions in France: fresh evidence using asymmetric cointegration. Environ. Sci. Pollut. Res. 30, 13224–13245. https://doi.org/10.1007/s11356-022-22958-1

Pinho, S.P., Macedo, E.A., 2005. Solubility of NaCl, NaBr, and KCl in Water, Methanol, Ethanol, and Their Mixed Solvents. J. Chem. Eng. Data 50, 29–32. https://doi.org/10.1021/je049922y

Plimpton, S., 1995. Fast Parallel Algorithms for Short-Range Molecular Dynamics. J. Comput. Phys. 117, 1–19. https://doi.org/10.1006/jcph.1995.1039

Preter, P. de, 2002. SAFIR-2 and the Belgian methodological R and D programme on deep disposal. Nuclear Energy Agency of the OECD (NEA).

Qiu, J., Jiang, S., Wang, Y., Chen, G., Liu, D., Liu, X., Wang, G., Wu, P., Lyu, X., 2020. Crystal chemistry characteristics and dispersion performance of Ca-montmorillonite with different layer charge density. Mater. Res. Express 7, 075505. https://doi.org/10.1088/2053-1591/aba803

Ramírez, S., Vieillard, P., Bouchet, A., Cassagnabère, A., Meunier, A., Jacquot, E., 2005. Alteration of the Callovo–Oxfordian clay from Meuse-Haute Marne underground laboratory (France) by alkaline solution. I. A XRD and CEC study. Appl. Geochem. 20, 89–99. https://doi.org/10.1016/j.apgeochem.2004.03.009

Rotenberg, B., 2007. Water and ions in clays : Unraveling the interlayer/micropore exchange using molecular dynamics. Geochim. Cosmochim. Acta. https://doi.org/10.1016/j.gca.2007.08.018

Rotenberg, B., Marry, V., Malikova, N., Turq, P., 2010. Molecular simulation of aqueous solutions at clay surfaces. J. Phys. Condens. Matter 22, 284114. https://doi.org/10.1088/0953-8984/22/28/284114

Ryckaert, J.-P., Ciccotti, G., Berendsen, H.J.C., 1977. Numerical integration of the cartesian equations of motion of a system with constraints: molecular dynamics of n-alkanes. J. Comput. Phys. 23, 327–341. https://doi.org/10.1016/0021-9991(77)90098-5

Smith, D.E., Dang, L.X., 1994. Computer simulations of NaCl association in polarizable water. J. Chem. Phys. 100, 3757–3766. https://doi.org/10.1063/1.466363

Sun, L., Hirvi, J.T., Schatz, T., Kasa, S., Pakkanen, T.A., 2015. Estimation of Montmorillonite Swelling Pressure: A Molecular Dynamics Approach. J. Phys. Chem. C. https://doi.org/10.1021/acs.jpcc.5b04972

Ta, A.T., Ullberg, R.S., Phillpot, S.R., 2023. Surface Reconstruction and Cleavage of Phyllosilicate Clay Edge by Density Functional Theory. Appl. Clay Sci. 246, 107178. https://doi.org/10.1016/j.clay.2023.107178

Thompson, A.P., Aktulga, H.M., Berger, R., Bolintineanu, D.S., Brown, W.M., Crozier, P.S., in 't Veld, P.J., Kohlmeyer, A., Moore, S.G., Nguyen, T.D., Shan, R., Stevens, M.J., Tranchida, J., Trott, C., Plimpton, S.J., 2022. LAMMPS - a flexible simulation tool for particle-based materials modeling at the atomic, meso, and continuum scales. Comput. Phys. Commun. 271, 108171. https://doi.org/10.1016/j.cpc.2021.108171

Tournassat, C., Bourg, IanC., Holmboe, M., Sposito, G., Steefel, CarlI., 2016. Molecular Dynamics Simulations of Anion Exclusion in Clay Interlayer Nanopores. Clays Clay Miner. 64, 374–388. https://doi.org/10.1346/CCMN.2016.0640403

Van Olphen, H., 1991. An introduction to clay colloid chemistry : for clay technologists, geologists, and soil scientists, 2nd ed. Krieger Pub. Co.

Wall, N.A., Maulden, E., Gager, E.J., Ta, A.T., Ullberg, R.S., Zeng, G., Nava-Farias, L., Sims, A.P., Nino, J.C., Phillpot, S.R., Szecsody, J.E., Pearce, C.I., 2022. Functionalized Clays for Radionuclide Sequestration: A Review. ACS Earth Space Chem. 6, 2552–2574. https://doi.org/10.1021/acsearthspacechem.2c00098

Wang, Z., Liu, L., 2012. A density functional study of the swelling behaviors of Na-bentonite. Presented at the Clays in natural and engineered barriers for radioactive waste confinement - 5 International meeting Book of abstracts, France, p. 923.

White, G.N., 1988. Analysis and Implications of the Edge Structure of Dioctahedral Phyllosilicates. Clays Clay Miner. 36, 141–146. https://doi.org/10.1346/CCMN.1988.0360207

Zheng, X., Underwood, T.R., Bourg, I.C., 2023. Molecular dynamics simulation of thermal, hydraulic, and mechanical properties of bentonite clay at 298 to 373 K. Appl. Clay Sci. 240, 106964. https://doi.org/10.1016/j.clay.2023.106964

Zhu, L., Sheng, D., Xu, C., Dai, X., Silver, M.A., Li, J., Li, P., Wang, Yaxing, Wang, Yanlong, Chen, L., Xiao, C., Chen, J., Zhou, R., Zhang, C., Farha, O.K., Chai, Z., Albrecht-Schmitt, T.E., Wang, S., 2017. Identifying the Recognition Site for Selective Trapping of 99TcO4– in a Hydrolytically Stable and Radiation Resistant Cationic Metal–Organic Framework. J. Am. Chem. Soc. 139, 14873–14876. https://doi.org/10.1021/jacs.7b08632